MODELLISTICA E CALCOLO SCIENTIFICO

MOX

MODELING AND SCIENTIFIC COMPUTING

MOX-Report No. 45/2019

Active force generation in cardiac muscle cells: mathematical modeling and numerical simulation of the actin-myosin interaction

Regazzoni, F.; Dedè, L.; Quarteroni, A.

Active force generation in cardiac muscle cells: mathematical modeling and numerical simulation of the actin-myosin interaction

F. Regazzoni[1], L. Dedè[1], and A. Quarteroni[1,2]

[1]MOX - Dipartimento di Matematica, Politecnico di Milano,
P.zza Leonardo da Vinci 32, 20133 Milano, Italy
[2]Mathematics Institute, École Polytechnique Fédérale de Lausanne,
Av. Piccard, CH-1015 Lausanne, Switzerland (*Professor Emeritus*)

Abstract

Cardiac in silico numerical simulations are based on mathematical models describing the physical processes involved in the heart function. In this review paper, we critically survey biophysical detailed mathematical models describing the subcellular mechanisms behind mechanical activation, that is the process by which the chemical energy of ATP (adenosine triphosphate) is transformed into mechanical work, thus making the muscle tissue contract. While presenting these models, that feature different levels of biophysical detail, we analyze the trade-off between the accuracy in the description of the subcellular mechanisms and the number of parameters that need to be estimated from experiments. Then, we focus on a generalized version of the classic Huxley model, that is able of reproducing the main experimental characterizations associated to the time scales typical of an heartbeat – such as the force-velocity relationship and the tissue stiffness in response to small steps – featuring only four independent parameters. Finally, we show how those parameters can be calibrated starting from macroscopic measurements available from experiments.

Keywords Mathematical modeling, Cardiac modeling, Active stress, Sarcomeres, Crossbridges

1 Introduction

Cardiovascular diseases represent the worldwide leading causes of death (Murray et al. 2014), with millions of cases every year. While advancements in medical practice are continuously leading to the development of new therapies and to the improvement of patients care, the role of mathematical and numerical modeling and, more generally, computational medicine, is increasingly being recognized in the context of cardiovascular research. Realistic and accurate in silico models can indeed provide valuable insights on the heart function and support clinicians for personalized treatment of patients (Smith et al. 2004; Crampin et al. 2004; Nordsletten et al. 2011; Fink et al. 2011; Chabiniok et al. 2016; Gerbi, Dedè, and Quarteroni 2018; Quarteroni et al. 2019).

The development of a mathematical and numerical model of the heart function requires integrating together models describing the different physical processes involved, at different spatial scales, in the cardiac activity. The heart is indeed a *multiphysics* and *multiscale* system, whose functions is the result of multiple processes acting in concert to accomplish its main goal, that is pumping blood throughout the body, to supply organs with oxygen and nutrients and to remove the metabolic waste (Tortora and Derrickson 2008; Jenkins, Kemnitz, and Tortora 2007; Katz 2010; Bers 2001). This process involves an electrophysiological activity (the propagation of an electric potential throughout the cardiac cells membrane and ionic exchanges across the membrane), a subcellular activity (the interactions of contractile proteins) and a mechanical activity (the contraction of the muscle and the resulting blood ejection form the cardiac chambers).

Each process involved in the cardiac function can be described by ad hoc developed mathematical models, written in different forms, including:

- systems of ODEs (Ordinary Differential Equations, see e.g. Hodgkin and Huxley 1952; Ten Tusscher et al. 2004; Ten Tusscher and Panfilov 2006; Aliev and Panfilov 1996; Bueno-Orovio, Cherry, and Fenton 2008; Regazzoni, Dedè, and Quarteroni 2018; Regazzoni, Dedè, and Quarteroni 2019; Regazzoni 2019; Hunter, McCulloch, and Ter Keurs 1998; Niederer, Hunter, and Smith 2006; Land et al. 2012);

- systems of PDEs (Partial Differential Equations, see e.g. Colli Franzone, Pavarino, and Savaré 2006; Colli Franzone, Pavarino, and Scacchi 2014; Guccione, McCulloch, and Waldman 1991; Holzapfel and Ogden 2009; Huxley 1957; Regazzoni 2019);

- continuous-time Markov Chains (see e.g. Rice et al. 2003; Hussan, Tombe, and Rice 2006; Sugiura et al. 2012; Washio et al. 2013; Washio et al. 2015);

- systems of SDEs (Stochastic Differential Equations, see e.g. Caruel and Truskinovsky 2018; Caruel, Moreau, and Chapelle 2019).

In this review paper, we focus on the models describing the subcellular processes by which the energy stored in ATP is transformed into mechanical work, thus leading to the contraction of the myocardium. To fulfill their predictive role, these mathematical models should accurately describe the complex mechanisms involved in the process of active force generation. However, very detailed models typically feature large numbers of parameters, which need to be estimated by experimental measurements. The difficulty inherent to direct measures of the subcellular properties of the cardiac tissue calls for a difficult trade-off between the biophysical detail of the models and the identifiability of their parameters.

1.1 Paper outline

This paper is organized as follows. In Sec. 2 we illustrate the physiological basis of the active contraction of the cardiac muscle and the main experimental characterizations of this phenomenon, and we highlight the fundamental behaviors that need to be reproduced by mathematical models. Then, in Sec. 3, we review several mathematical models, available in literature, describing the mechanisms by which force is generated in the cardiac muscle. In Sec. 4 we consider the issue of parameters identifiability for force generation models. In particular, we show, for a modified version of the Huxley
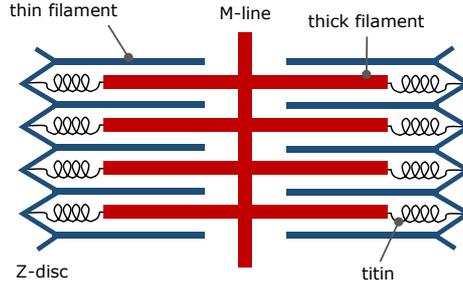
Figure 1: Representation of a sarcomere. Inside sarcomeres, thin and thick filaments are arranged with a regular structure. *M-lines*, located at the center of the sarcomere, have the function of connecting thick filaments together. *Z-discs* link adjacent sarcomeres to each other and to the extracellular matrix and are connected to thick filaments through a huge cytoskeletal protein named *titin*.

model (Huxley 1957), how the model parameters can be estimated by measurement typically available from experiments. Finally, in Sec. 5, we discuss some concluding remarks.

2 Active force generation in the cardiac tissue

Sarcomeres, the fundamental contractile units of striated (i.e. skeletal and cardiac) muscles, have a cylindrical shape, with a length ranging from $1.7\,\mu$m and $2.3\,\mu$m in physiological conditions. They mainly consists in two types of filaments, thin filaments (or actin filaments, AF) and thick filaments (myosin filaments, MF), arranged with a nearly crystalline structure (see Fig. 1). Active force is generated by the interaction of the protein actin, located on the thin filament, and the protein myosin, located in the thick filaments (Tortora and Derrickson 2008; Jenkins, Kemnitz, and Tortora 2007; Katz 2010; Bers 2001).

The contraction of sarcomeres is triggered by an increase of intracellular calcium ions concentration and can be split into two steps. The first one is the *thin filament regulation*, the second one is the *actomyosin interaction*. The focus of this paper is on the second of the two steps, described in Sec. 2.1.

In the first step, calcium ions bind to the so-called regulatory units (troponin-tropomyosin complexes located on the thin filaments), thus inducing a conformational change in tropomyosin. Tropomyosin acts as an on-off switch for the actomyosin interaction: when it is in non-permissive state, it sterically hinders the binding of myosin with the regulated actin binding sites. Conversely when a tropomyosin unit is in permissive state, the regulated actin binding sites are free to interact with myosin and to generate force. The actomyosin interaction is a cyclical process, known as *Lymn-Taylor cycle* (Lymn and Taylor 1971), described in detail in the next section (Sec. 2.1).

2.1 The Lymn-Taylor cycle

Myosin is a molecule made of a coiled–coil tail and two paired heads, capable of binding to actin, thus forming the so-called crossbridges (XBs). Myosin is indeed a

3
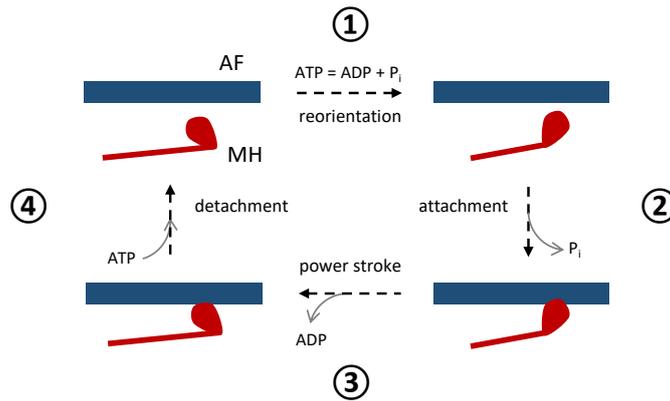
Figure 2: Representation of the Lymn-Taylor cycle.

molecular motor, which translates the chemical energy stored inside ATP, the primary energy carrier in living organisms, into mechanical work. This is made possible by the so–called *power-stroke*, that is a rotation of the attached myosin heads (MHs) which pulls the AF towards the centre of the sarcomere. After the power-stroke, the MH detaches and binds to actin in a different position and the cycle is repeated. The joint work of several thousands of pulling MHs makes the sarcomere contract (Tortora and Derrickson 2008; Jenkins, Kemnitz, and Tortora 2007; Katz 2010; Bers 2001).

Such attachment-detachment process takes place along a cyclical path, described by the Lymn-Taylor cycle, comprising the following four steps (Lymn and Taylor 1971; Bers 2001; Keener and Sneyd 2009; Caruel and Truskinovsky 2018), represented in Fig. 2.

1. **ATP hydrolisis.** Myosin, in the stage of the cycle that is traditionally considered as the starting point, is bound to ATP and detached from actin. The catalytic site of myosin hydrolyses ATP into ADP and a phosphate group P_i (which remains attached to myosin), transferring to myosin the energy stored in ATP. The MH is still detached from actin, but reoriented and in a higher energetic state.

2. **XB attachment.** The energized MH binds to actin and the phosphate group is released.

3. **Power stroke.** The MH rotates towards the centre of the sarcomere (less energetic state), thus pulling the actin filament in the same direction. ADP is released from myosin. The force developed by a single power stroke is nearly 0.5–1.0 pN, and the head rotation is nearly 5–10 nm.

4. **XB detachment.** At the end of the power stroke, myosin is tightly bound to actin in a *rigor* configuration, until an ATP molecule binds to myosin, making it detach from actin.

The Lymn-Taylor cycle is repeated, with a pace of nearly five times per second, as long as two conditions are satisfied: enough ATP to fuel the process is available; calcium ions level is high enough to keep tropomyosin in the permissive configuration. When ATP is depleted, the cycle stops in the phase between steps 3 and 4, where all XBs are firmly attached (leading, for skeletal muscle, to the *rigor* state observed in cadavers).

(a) Force-velocity relatioship   (b) Fast transient response
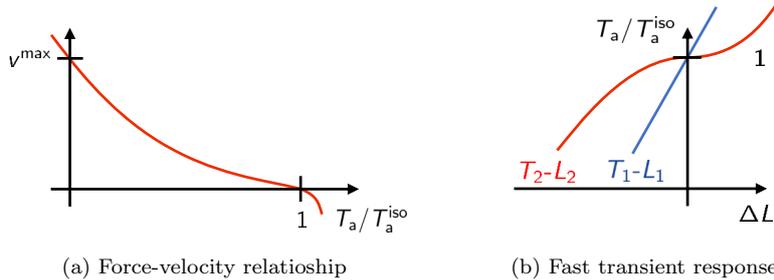
Figure 3: Representation of the force-velocity curve (a) and tension-elongation curves after a fast transient (b) that is typically obtained in experiments.

When calcium concentration returns to its rest concentration, instead, the cycle is stopped in the phase between steps 1 and 2.

2.2 Force-velocity relationship

One of the earliest experimental characterizations of muscle functionality is the force-velocity relationship, dating back to Archibald V. Hill, Nobel Prize winner for his work on the heat production and mechanical work in muscles (Hill 1938). In the Hill's experimental setup, a muscle fiber is stimulated under isometric conditions until it reaches the steady-state active tension T_a^{iso}. Then, a negative (or positive) force step is applied. After a transient phase (which is discussed in Sec. 2.3), the fiber reaches a steady-state with a constant shortening (or lengthening) velocity. The measured force-velocity relationship is a convex curve for positive shortening velocities, connecting the so-called *stall force*, namely the force in isometric conditions (T_a^{iso}), with the *maximum shortening velocity* (v^{max}), in correspondence of which the generated tension is zero (see Fig. 3a).

The force in isometric conditions T_a^{iso} depends on two variables (the sarcomere length SL and the calcium concentration inside the cells $[Ca^{2+}]_i$, where the subscript "i" stands for *intracellular*) that affect the fraction of permissive regulatory units (Bers 2001; Katz 2010). Clearly, also the force-velocity curves are affected by the same variables; however, when the tension is normalized with respect to the isometric values, the curves obtained with different values virtually superimpose (Bers 2001; Caremani et al. 2016). This observation suggests that the mechanism underlying the force-velocity relationship is largely independent of the calcium-driven regulation and, therefore, it is linked to the cycling of XBs (Keener and Sneyd 2009; Caruel and Truskinovsky 2018; Caremani et al. 2016). The maximum shortening velocity for half-sarcomere is independent on the $[Ca^{2+}]_i$ and SL and it is about $v_{hs}^{max} = 8\,\mu m\,s^{-1}$ (significantly larger than for skeletal muscle).

2.3 Fast isometric and isotonic transients

Fast isometric and isotonic experiments help shedding light on the fastest time scales involved in the dynamics of force generation in the muscle tissue. The two experimental setups are briefly described in the following.

- **Force clamp** (soft device or isotonic transient). It consists in the same setup employed to obtain the force-velocity relationship. After the isometric force is

reached, a step in tension is applied. After a fast transient, the fiber reaches a constant velocity.

- **Length clamp** (hard device or isometric transient). In this case, after that the steady-state is reached while keeping constant the length of the fibers (typically in the range of sarcomere lengths for which the force-length curve is constant, Gordon, Huxley, and Julian 1966; Kentish et al. 1986; Ter Keurs, Hollander, and Keurs 2000), a step in length is applied (without exiting the above mentioned plateau region). The measured force undergoes a fast transient, before returning to the original level.

In both the cases, the observed transient can be split into four different phases (even if in the cardiac tissue the third phase is absent), associated with different time scales (Keener and Sneyd 2009; Marcucci and Truskinovsky 2010a; Marcucci and Truskinovsky 2010b; Caruel and Truskinovsky 2018; Caremani et al. 2016).

- **Phase 1** ($\sim 200\,\mu s$). In a first phase the tension T (respectively, the length of the fiber L) changes simultaneously with the step in L (respectively, in T), until it reaches a level called T_1 (respectively, L_1). Interestingly, by plotting the values of T_1 and L_1 in the T-L plane, the curves obtained with the soft and hard devices superimpose and show a linear relationship between tension and elongation (Fig. 3b). This first phase of the transient is indeed linked to the instantaneous elastic response of XBs. Measurements of the stiffness of this relationship under *rigor* conditions (when the number of attached XBs can be estimated) allow to estimate the stiffness of a single XB (Piazzesi et al. 2007).

- **Phase 2** ($\sim 2 - 3\,ms$). After the instantaneous response, tension (respectively, length) quickly reaches a second level, denoted by T_2 (respectively, L_2). Also in this case, the curves of T_2-L_2 obtained with the soft and hard devices superimpose. For lengths close to the rest length, the T_2 tension is very similar to the isometric tension T_a^{iso}, but for larger length steps it is approximately linear in L, with a lower stiffness than the elastic stiffness, related to T_1 (Fig. 3b). The time scale associated with this phase coincides with the time scale of the power stroke: in this phase, MHs rearrange from the non-equilibrium condition due to the fast step in length until a new equilibrium is reached. Indeed, for small length steps, the power stroke is sufficient for the fibers to almost recover the initial tension level T_a^{iso}.

- **Phase 3 and 4** ($\sim 500\,ms$). After the rapid second phase, in length clamp experiments tension slowly recovers its original level T_a^{iso} (if the step in length is such that the sarcomeres are still in the plateau region of the force-length relationship). In force clamp experiments, as described in Sec. 2.2, the filament reaches a steady-state with a constant shortening (or lengthening) velocity. Such velocity, plotted against the isotonic tension, gives the force-velocity curve. This final phase is associated with the XBs attachment and detachment, the slower step of the Lymn-Taylor cycle (see Sec. 2.1).

Similarly to the force-velocity relationship, when the tension is normalized with respect to the isometric values, the tension-elongation curves virtually superimpose (Caremani et al. 2016). This fact supports the hypothesis that the phenomena associated with the fast time scales observed through this experimental setup are linked to the XB dynamics, and not to the regulatory units dynamics.
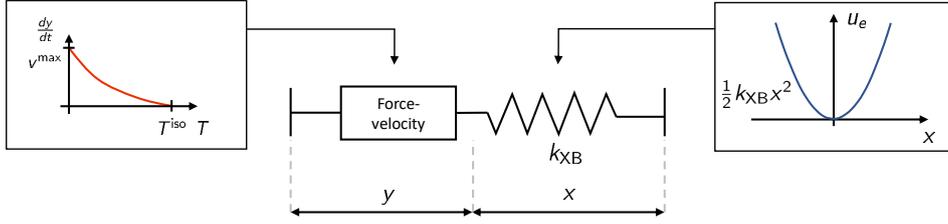
Figure 4: Sketch of the phenomenological model of Hill 1938. A contractile element, following the law (2), is coupled in series with an elastic element, to which a quadratic energy $u_e(x) = \frac{1}{2} k\, x^2$ is associated.

3 Mathematical models of the actomyosin interaction

In this section, we review several contributions available in literature to the definition of mathematical models describing the dynamics of XBs. The historical development of such models reflects the progresses in the understanding by the physiologists community of the mechanisms underlying the microscopic force generation. We notice that most of the models are suitable for both the skeletal and the cardiac muscle, provided that the parameters are calibrated accordingly.

3.1 Hill 1938 model

One of the earliest mathematical descriptions of muscles dates back to Hill 1938. By studying the release of heat when a muscle contracts against a constant load (isotonic contraction), A. V. Hill discovered that the relationship between the active tension T_{a} and the shortening velocity v_{fiber} is well described by the hyperbolic law:

$$(T_{\mathrm{a}} + a)\, v_{\mathrm{fiber}} = b_{\mathrm{fiber}}\, (T_{\mathrm{a}}^{\mathrm{iso}} - T_{\mathrm{a}}), \tag{1}$$

where $T_{\mathrm{a}}^{\mathrm{iso}}$ is the isometric tension (i.e. the tension for $v_{\mathrm{fiber}} = 0$), while a and b_{fiber} are positive constants. In the following, it will be helpful to write relationships that are independent of the length of the muscle fiber used to perform the experiment. With this aim, by dividing Eq. (1) by the length of the fiber L_{fiber}, we get the following relationship:

$$(T_{\mathrm{a}} + a)\, v = b\, (T_{\mathrm{a}}^{\mathrm{iso}} - T_{\mathrm{a}}). \tag{2}$$

where we call $v = v_{\mathrm{fiber}}/L_{\mathrm{fiber}}$ the *normalized velocity* (dimensionally, v is the inverse of time units). The maximum shortening velocity, that is the maximum speed at which the muscle is able to shorten (see Sec. 2.2), can be computed as $v^{\mathrm{max}} = b\, T_{\mathrm{a}}^{\mathrm{iso}}/a$. In the original paper, by fitting the experimental measurements, Hill obtained $a/T_{\mathrm{a}}^{\mathrm{iso}} = 0.22$, $b_{\mathrm{fiber}} = 1.03\,\mathrm{cm\,s^{-1}}$ for a fiber of length $L_{\mathrm{fiber}} = 38\,\mathrm{mm}$, thus $b = 0.27\,\mathrm{s^{-1}}$ and $v^{\mathrm{max}} = 1.23\,\mathrm{s^{-1}}$ (Hill 1938).

On the basis of the relationship (2), Hill proposed a phenomenological model where an elastic element is arranged in series with a contractile element governed by the law (2) itself. This model, however, does not provide any insight into the muscle functioning, as it is not based on a microscopical description of the tissue (this is not surprising since the muscle anatomy was not known at that time).

7

3.2 Huxley 1957 (H57) model

In 1957, A. F. Huxley proposed a model (H57 model) to link the force-velocity relationship observed by A. V. Hill with the subcellular attachment-detachment process of MHs (Huxley 1957). This model considers two states (bound and unbound) and assumes that the transition rates depend on the distance between the myosin arm rest position and the BS, denoted by x. We have $x > 0$ when the attachment leads to a positive tension, $x \leq 0$ otherwise (see Fig. 5).

Let us consider a population of MHs and BSs, and assume that the probability density of finding a couple with a given displacement x is constant in a an interval sufficiently close to $x = 0$ (more precisely, the number of couples with displacement $x \in (a, b)$ for each half filament is $\rho_{\mathrm{AM}}|b - a|$, if a and b are sufficiently close to 0). This is well motivated, assuming the effect of the units located at the border of the filaments negligible.

Let $n(x, t) \in [0, 1]$ denote the probability that a couple MH-BS with elongation x is attached. Then, the expected value of the number of attached XBs with elongation between a and b at time t is given by:

$$\rho_{\mathrm{AM}} \int_a^b n(x, t) dx.$$

Let us consider a small time interval Δt. The variation of the population of attached MHs from t to $t + \Delta t$ with displacement in the interval (a, b) is given (at the first order in Δt) by:

$$\int_a^b n(x, t + \Delta t) dx \sim \int_a^b n(x, t) dx + n(b, t) v_{\mathrm{hs}}(t) \Delta t - n(a, t) v_{\mathrm{hs}}(t) \Delta t$$
$$+ \int_a^b (1 - n(x, t)) f(x) \Delta t \, dx - \int_a^b n(x, t) g(x) \Delta t \, dx, \tag{3}$$

where $v_{\mathrm{hs}}(t) = -\frac{dSL(t)/2}{dt}$, the shortening velocity of half sarcomere (that is the relative velocity between the MF and the AF), convects the MH distribution and $f(x)$ and $g(x)$ are the attachment and detachment rates, respectively. By dividing the above equation by $\Delta t \, (b - a)$ and letting both intervals go to zero, we get the H57 model:

$$\frac{\partial n(x, t)}{\partial t} - v_{\mathrm{hs}}(t) \frac{\partial n(x, t)}{\partial x} = (1 - n(x, t)) f(x) - n(x, t) g(x), \qquad x \in \mathbb{R}, \, t \geq 0, \quad (4)$$

with suitable initial conditions. Finally, assuming that each attached XB acts as a linear spring with stiffness k_{XB}, the total force exerted by the pair of interacting half thick filament and thin filament is equal to:

$$F_{\mathrm{hf}}(t) = \rho_{\mathrm{AM}} \, k_{\mathrm{XB}} \int_{-\infty}^{+\infty} x \, n(x, t) dx. \tag{5}$$

In Huxley 1957, the transition rates are phenomenologically set as:

$$f(x) = f_1 \frac{x}{h} \mathbb{1}_{[0,h]}(x), \qquad g(x) = g_2 \mathbb{1}_{x \leq 0} + g_1 \frac{x}{h} \mathbb{1}_{x > 0}, \tag{6}$$

where f_1, g_1 and g_2 are positive constants. Attachment can occur only in the interval $x \in [0, h]$, that is for positive displacement: such symmetry-breaking feature is what makes the muscle contract. For $x < 0$ the detachment rate is very high, in order to prevent the XBs to generate force in the opposite direction.
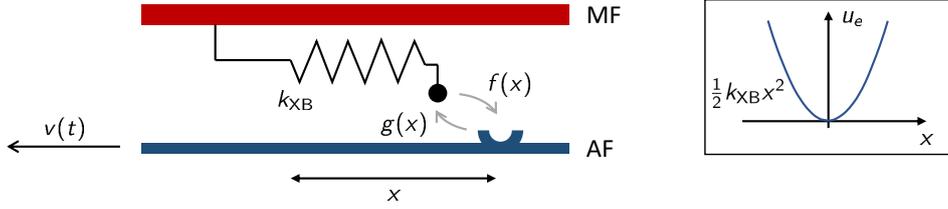
Figure 5: Scheme of the H57 model. The attachment-detachment rates of MHs (denoted respectively by f and g) depend on the XB distortion x. The myosin arm is modeled as a linear elastic element with stiffness k_{XB}.

The H57 model provides a microscopical explanation of the force-velocity relationship. When the shortening velocity is high, the attached XBs are convected towards lower values of x, thus leading to a reduction of force. This mechanism is often compared to a "tug-of-war" game. If the rod is quickly pulled, the players need to detach their hands and reattach them further on the rod, otherwise they are not able to pull any more. Thus, when the rod is sliding towards to players, their action is less efficient than in the steady regime, when they can firmly hold the rod. It is all about how fast the rod slides and how are the players fast in detaching and reattaching their hands. We will see later a quantitative description of the competition between the two phenomena.

With the choice (6), Huxley derived a steady-state solution (with a constant shortening velocity) for (4):

$$
n(x) = \begin{cases} F_1 \left(1 - e^{-\varphi/v_{\mathrm{hs}}}\right) e^{\frac{x}{2h} G_2 \frac{\varphi}{v_{\mathrm{hs}}}} & x < 0, \\ F_1 \left(1 - e^{\left(\frac{x^2}{h^2} - 1\right) \frac{\varphi}{v_{\mathrm{hs}}}}\right) & 0 \le x < h, \\ 0 & x \ge h, \end{cases} \tag{7}
$$

where $\varphi = (f_1 + g_1)h/2$, $F_2 = \frac{f_1}{f_1 + g_1}$, $G_2 = \frac{g_2}{f_1 + g_1}$. This gives the following force-velocity relationship:

$$
F_{\mathrm{hf}} = \rho_{\mathrm{AM}} k_{\mathrm{XB}} F_1 \frac{h^2}{2} \left(1 - \frac{v_{\mathrm{hs}}}{\varphi} \left(1 - e^{-\varphi/v_{\mathrm{hs}}}\right) \left(1 + \frac{1}{2G_2^2} \frac{v_{\mathrm{hs}}}{\varphi}\right)\right). \tag{8}
$$

Huxley, proceeding by trial and error, obtained a good fit of experimental data with $F_1 = 13/16$ and $G_2 = 3.919$. For this parameters, by setting $F_{\mathrm{hf}} = 0$ we have $v_{\mathrm{hs}}^{\max} \simeq 4\varphi$. For instance, in Brokaw 1976, with the choice $f_1 = 65\,\mathrm{s}^{-1}$, $g_1 = 15\,\mathrm{s}^{-1}$, $g_1 = 313.5\,\mathrm{s}^{-1}$, $h = 10\,\mathrm{nm}$, one gets $v_{\mathrm{hs}}^{\max} \simeq 1600\,\mathrm{nm\,s}^{-1}$, which gives $v^{\max} = v_{\mathrm{hs}}^{\max}/(SL_0/2) \simeq 1.45\,\mathrm{s}^{-1}$, were we denote by SL_0 the reference sarcomere length. All the above mentioned constants are calibrated for the skeletal muscle.

3.2.1 The distribution-moment equations

To avoid the solution of a PDE, in Zahalak 1981 an approximation of the model (4) by means of ODEs was proposed. By applying a general strategy of statistical physics, the author computed the equations for the evolution of the distribution-moments of $n(x, t)$, defined as:

$$
\mu^p(t) := \int_{-\infty}^{+\infty} x^p n(x, t) dx.
$$

9

Indeed, thanks to the linear spring hypothesis for the myosin arm, the full distribution $n(x,t)$ is not needed to compute the force, but rather its first moment is enough, as we have, from Eq. (5):

$$F_{\mathrm{hf}}(t) = \rho_{\mathrm{AM}} \, k_{\mathrm{XB}} \, \mu^1(t). \tag{9}$$

By multiplying Eq. (4) by x^p and integrating over $(-\infty, +\infty)$ one gets, for $p = 0, 1, \ldots$:

$$\frac{d}{dt} \mu^p(t) - p \, v_{\mathrm{hs}}(t) \, \mu^{p-1}(t) = \mu_f^p - \int_{-\infty}^{+\infty} x^p (f(x) + g(x)) n(x,t) dx, \tag{10}$$

where we have integrated by parts the term

$$\int_{-\infty}^{+\infty} x^p \frac{\partial n(x,t)}{\partial x} dx = [x^p \, n(x,t)]_{-\infty}^{+\infty} - p \int_{-\infty}^{+\infty} x^{p-1} n(x,t) dx = -p \, \mu^{p-1}(t),$$

and we have used the fact that $n(-\infty, t) = n(+\infty, t) = 0$. The last term of (10) needs to be modeled for model closure. In Zahalak 1981 the authors proposed to assume a specific distribution (a gaussian distribution) for $n(\cdot, t)$, so that that term can be computed. Specifically, by assuming that:

$$n(x,t) = \frac{\mu^0(t)}{\sqrt{2\pi}\sigma(t)} \exp\left(-\frac{(x - \bar{x}(t))^2}{2\sigma^2(t)}\right),$$

where

$$\bar{x}(t) = \frac{\mu^1(t)}{\mu^0(t)}, \quad \sigma^2(t) = \frac{\mu^2(t)}{\mu^0(t)} - \left(\frac{\mu^1(t)}{\mu^0(t)}\right)^2,$$

the distribution $n(\cdot, t)$ is fully characterized by its first three moments, and thus the first three equations of (10) are completely equivalent to the PDE model (4). However, we have here to pay the price of a strong assumption of gaussianity for $n(\cdot, t)$. Still, the analytical solution of Eq. (7) shows that even in the steady-state case the distribution may be very skewed and thus significantly differ from a gaussian one.

When the transition rates $f(x)$ and $g(x)$ take special forms, the distribution-moments strategy can be used to derive exact equivalents of the PDE model (4) (Bestel, Clément, and Sorine 2001; Chapelle et al. 2012). In fact, if the total transition rate is independent of the displacement (i.e. $f(x) + g(x) = r$), the last term in (10) can be computed as:

$$\int_{-\infty}^{+\infty} x^p (f(x) + g(x)) n(x,t) dx = r\mu^p(t),$$

and the hierarchy of equations (10) can be truncated by considering only the first two moments:

$$\begin{cases} \dfrac{d}{dt} \mu^0(t) = \mu_f^0 - r \, \mu^0(t) & t \geq 0, \\ \dfrac{d}{dt} \mu^1(t) = \mu_f^1 - r \, \mu^1(t) + v_{\mathrm{hs}}(t) \, \mu^0(t) & t \geq 0. \end{cases} \tag{11}$$

3.2.2 Extensions of the H57 model

To account for the fact that not all XBs can be recruitable for attachment (e.g. because a portion of the MF does not face any AF), in Chapelle et al. 2012 the authors modified the source term $(1 - n(x,t))f(x)$ of (4) into $(n_0(t) - n(x,t))f(x)$, where the reduction factor $0 \leq n_0(t) \leq 1$ denotes the fraction of recruitable XBs.

In Bestel, Clément, and Sorine 2001; Chapelle et al. 2012 the authors introduced a chemical input, affecting the transition rates $f(x)$ and $g(x)$, to model the effect of the calcium-driven regulation. Moreover, by assuming that high relative velocities between the two filaments can lead to destruction of XBs, they introduced a further sink term, linearly proportional to $|v(t)|$. Specifically, the following transition rates were chosen:

$$f(x,t) = k_{\text{ATP}} \mathbb{1}_{x \in [0,1]} \mathbb{1}_{[\text{Ca}^{2+}]_{\text{i}}(t) > C},$$
$$g(x,t) = k_{\text{ATP}} \mathbb{1}_{x \notin [0,1]} \mathbb{1}_{[\text{Ca}^{2+}]_{\text{i}}(t) > C} + k_{\text{RS}} \mathbb{1}_{[\text{Ca}^{2+}]_{\text{i}}(t) \leq C} + \alpha |v(t)|,$$

where k_{ATP} is the ATP turnover rate, C is the activation threshold for $[\text{Ca}^{2+}]_{\text{i}}$ and α is a positive constant. Despite the introduction of the dependence on $[\text{Ca}^{2+}]_{\text{i}}(t)$ and $v(t)$, the sum $f(x,t) + g(x,t)$ is still independent of x. Hence, distribution-moment equations analogous to (11) can be derived for this model.

In Kimmig et al. 2019 and Kimmig 2019 the authors proposed a model, based on the H57 formalism, where the population of MHs is split into two pools: the first one contains the MHs located in the single-overlap zone, while the other one (for which $f = 0$) contains the remaining MHs. Each pool is characterized by its own density function $n(x,t)$, whose evolution is described by an equation similar to Eq. (4), supplemented with a source and a sink term accounting for fluxes across the two pools. Moreover, a variable representing the fraction of permissive BSs multiplies to attachment rate term.

3.2.3 Limitations of the H57 model

The models belonging to the family of the H57 model, however, are not able to explain some of the phenomena experimentally observed. In particular, they fail to reproduce the phenomena related to time scales that are faster than the time scale of the power-stroke ($\sim 1\,\text{ms}$). The reason is that this class of models does not incorporate a description of the power-stroke, but rather assumes that MHs attach in a stretched configuration. This cannot explain the fast force recovery following a sudden change in the sarcomere length (see Sec. 2.3) since, in the H57 model, force is recovered with a time scale that is compatible with the ATP turnover (order of $100\,\text{ms}$). These limitations were recognized by A. F. Huxley himself, who proposed, in 1971, a model incorporating an explicit description of the power-stroke.

3.3 Power-stroke models

In Huxley and Simmons 1971 the authors proposed a new model (HS71 model), by interpreting the pre-power-stroke and the post-power-stroke configurations as discrete states. Thus, they introduced a degree of freedom, y, that can be interpreted as the angular position of the rotating MH. The variable y is associated with a discrete energy potential, with two minima in 0 and a (where a is the power-stroke length), separated by an energy barrier. This newly introduced degree of freedom supplements the linear elastic element of the H57, with potential energy $u_e(x) = k_{\text{XB}}/2\,(x+y)^2$.

This *hard-spin* model provided a first quantitative description of the power-stroke, with the assumption that the fast force recovery (see Sec. 2.3) is a passive mechanisms, interpretable as a mechanical conformational change. This is coherent with the observation that the fast force recovery is not rate limited by the chemical stages, supporting the hypothesis that the power-stroke is a mechanical phenomenon.

The main drawback of the hard-spin HS71 model is that the transition between the two configurations requires the linear spring to be stretched by the effect of thermal fluctuation in order to overcome the energy barrier. As a consequence, this model predicts a slower time-constant for the power-stroke than what is measured in experiments (Caruel 2011; Caruel and Truskinovsky 2018). This led to assume the existence of intermediate configurations, by the introduction of a number of additional states (Huxley and Simmons 1971; Smith et al. 2008).

In Washio et al. 2013; Washio et al. 2015, the authors considered a full-sarcomere model where the actomyosin interaction is described within the HS71 formalism, that is to say as transitions between discrete states. A continuous variable describing the myosin arm stretch is associated with each MH, so that the transition rates are made dependent on the XB distortion. Due to the complexity of the model, that also includes a description of the regulatory units, its solution is approximated by means of the Monte Carlo method. A similar model, where the crossbridge dynamics is described with a H71-like model, is proposed in Hussan, Tombe, and Rice 2006. In such models, additional states (besides the two states of the H71 model) are considered.

3.3.1 Soft-spin models

In contrast, in Marcucci and Truskinovsky 2010a; Marcucci and Truskinovsky 2010b the authors proposed to replace the rigid bistable device (or multi-stable) of hard-spin models by a bistable element, parametrized by a continuous variable. The transition from hard-spin to soft-spin removed the contradictions concerning the time scale of the power-stroke (Caruel and Truskinovsky 2018).

This model was extended with the inclusion of the attachment-detachement ATP-driven mechanism by adding a coloured noise (mimicking the out-of-equilibrium ATP reactions) to the Langevin dynamics within the energy landscape (Marcucci and Truskinovsky 2010b).

In Caruel, Moireau, and Chapelle 2019 the authors proposed a mechano-chemical model (CMC19 model), with a soft-spin model for MHs coupled with a chemical state describing the ATP-driven attachment-detachment process, obtaining a unified framework capable of matching both the phenomena related to the power-stroke (such as the fast velocity recovery) and those related to the attachment-detachment of XBs (such as the force-velocity curve). Moreover, the authors showed that the H57 model can be derived from the CMC19 model under simplifying assumptions, thus giving an interpretation to the H57 model in terms of Langevin dynamics. Remarkably, the authors also showed that a lumped version of the CMC19 model in which the power-stroke variable is assumed to be in equilibrium formally reduces to a H57-like model, thus allowing to interpret the transition rates of the H57 model as *effective* rates, in light of the CMC19 model. We illustrate in what follows the construction of the CMC19 model.

3.3.2 Caruel-Moireau-Chapelle 2019 (CMC19) model

Model setup. We consider a single MH, described by a discrete degree of freedom, namely ω^t ($\omega^t = 1$ when the MH is attached, $\omega^t = 0$ when it is detached), and two continuous degrees of freedom, namely Z^t (measuring the distance of the MH tip from the rest-position of the myosin harm) and Y^t (associated with the angular orientation of the MH), as it is shown in Fig. 6. In the pre-power-stroke configuration, we typically have $Y^t = 0$, and thus the elongation of the myosin arm coincides with Z^t. When power-stroke occurs, Y^t becomes positive, making the total myosin arm
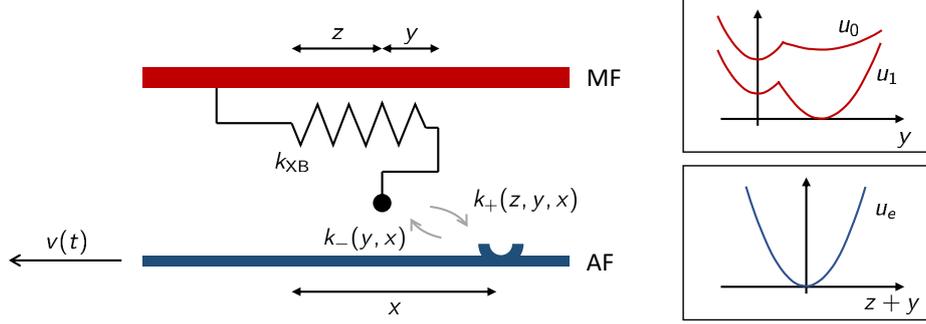
Figure 6: Scheme of the CMC19 model. The MH is described by two degrees of freedom (z and y). When the MH is attached, the degree of freedom z coincides with the variable x. The attachment-detachment rates of MHs (f and g) depend on the XB distortion x. The myosin arm is modeled as a linear elastic element with stiffness k_{XB}, while the degree of freedom y is associated with a bistable energy, which depends on the XB attachment state.

elogation increase. The myosin arm elogation is indeed given by $X^t + Y^t$ (see Fig. 6). When the MH is attached ($\omega^t = 1$) the tip of the MH is attached to the BS. Therefore, we have by definition $Z^t \equiv x$ (where we denote by x, as in the previous sections, the distance between to myosin arm rest position and the BS).

The elastic element is associated with a quadratic energy u_e, while the internal degree of freedom Y^t is associated with a bistable energy u_ω, that takes different expression when the XB is attached and when instead is not. Specifically, in the attached (respectively, detached) configuration, the minimum corresponding to the post-power-stroke configuration ($Y^t > 0$) is endowed with a lower (respectively, higher) energy than the pre-power-stroke configuration ($Y^t = 0$). The resulting energy landscape for the mechanical variables (Z^t, Y^t) is thus associated with the energy $w_\omega(z, y) = u_\omega(y) + u_e(z + y)$.

The Langevin dynamics (see e.g. Karatzas and Shreve 1998) associated with the energy $w_\omega(z, y)$ gives the following stochastic differential equation:

$$\begin{cases} \eta\, dZ^t = \left(-\omega^t \eta\, v_{\mathrm{hs}} - (1 - \omega^t) \dfrac{\partial w_\omega}{\partial z}(Z^t, Y^t) \right) dt \\ \qquad\quad + \eta \delta_{t_s}(t) \left(x - Z^t \right) dt + (1 - \omega^t) \sqrt{2\eta k_B T}\, dB_z^t \qquad t \geq 0, \\ \eta\, dY^t = -\dfrac{\partial w_\omega}{\partial y}(Z^t, Y^t) dt + \sqrt{2\eta k_B T}\, dB_y^t \qquad\qquad\qquad t \geq 0, \end{cases} \qquad (12)$$

where dB_z^t and dB_y^t are the increments of a two-dimensional Brownian motion, η is the viscous damping coefficient associated with the surrounding fluid, k_B denotes the Boltzmann constant, T the absolute temperature, and t_s denotes the time of any switch from $\omega^t = 0$ to $\omega^t = 1$. We notice that, far from $t = t_s$, when the XB is detached (i.e. $\omega^t = 0$), the first equation reduces to:

$$\eta dZ^t = -\frac{\partial w_\omega}{\partial z}(Z^t, Y^t) dt + \sqrt{2\eta k_B T}\, dB_z^t,$$

while when the XB is attached (i.e. $\omega^t = 1$), it reduces to:

$$dZ^t = -v_{\mathrm{hs}}\, dt,$$

13

coherently with the fact that $Z^t \equiv x$ (we recall that v_{hs} denotes the *shortening* velocity, thus $\dot{x} = -v_{\text{hs}}$). Finally, at time $t = t_s$ the Dirac delta term makes the variable Z^t instantaneously jump to $Z^t = x$.

The kinetics of the chemical degree of freedom ω^t is determined by the following transition rates:

$$
\begin{aligned}
\mathbb{P}\left[\omega^{t+\Delta t} = 1 | \omega^t = 0\right] &= k_+(Z^t, Y^t, x, t)\Delta t + o\left(\Delta t\right), \\
\mathbb{P}\left[\omega^{t+\Delta t} = 0 | \omega^t = 1\right] &= k_-(Y^t, x, t)\Delta t + o\left(\Delta t\right),
\end{aligned}
\tag{13}
$$

where the detachment transition rate is independent of Z^t since when the MH is attached we have $Z^t = x$.

Fokker-Plank equation. To write the Fokker-Plank equation (see e.g. Karatzas and Shreve 1998) associated with Eq. (12), we denote by $p(z, y, \omega; x, t)$ the probability density for a MH (at time t and located at distance x) of being in state (z, y, ω) (we notice that x and t are regarded as deterministic variables). Since for attached heads we have $Z^t = x$, the probability density for $\omega = 1$ can be written as:

$$
p(z, y, 1; x, t) = \delta_x(z)\bar{p}(y; x, t).
$$

With this notation, the Fokker-Plank equation reads:

$$
\begin{cases}
\begin{aligned}
\frac{\partial}{\partial t}p(z, y, 0; x, t) = {}& v_{\text{hs}}\frac{\partial}{\partial x}p(z, y, 0; x, t) \\
& + \eta^{-1}\frac{\partial}{\partial z}\left(\frac{\partial}{\partial z}w_0(z, y)\, p(z, y, 0; x, t)\right) \\
& + \eta^{-1}\frac{\partial}{\partial y}\left(\frac{\partial}{\partial y}w_0(z, y)\, p(z, y, 0; x, t)\right) \\
& + \frac{k_B T}{\eta}\left(\frac{\partial^2}{\partial z^2}p(z, y, 0; x, t) + \frac{\partial^2}{\partial y^2}p(z, y, 0; x, t)\right) \\
& + k_-(y, x)\delta_x(z)\bar{p}(y; x, t) \\
& - k_+(z, y, x)p(z, y, 0; x, t) \qquad\qquad x, y, z \in \mathbb{R},\ t > 0,
\end{aligned} \\
\begin{aligned}
\frac{\partial}{\partial t}\bar{p}(y; x, t) = {}& v_{\text{hs}}\frac{\partial}{\partial x}\bar{p}(y; x, t) \\
& + \eta^{-1}\frac{\partial}{\partial y}\left(\frac{\partial}{\partial y}w_1(x, y)\,\bar{p}(y; x, t)\right) \\
& + \frac{k_B T}{\eta}\frac{\partial^2}{\partial y^2}\bar{p}(y; x, t) \\
& + \int_{-\infty}^{+\infty} k_+(z, y, x)p(z, y, 0; x, t)dz \\
& - k_-(y, x)\bar{p}(y; x, t) \qquad\qquad\qquad\quad x, y \in \mathbb{R},\ t > 0,
\end{aligned}
\end{cases}
\tag{14}
$$

endowed with suitable initial conditions. To link this model with the H57 formalism, we notice that the fraction of attached MHs with displacement x at time t is given by:

$$
n(x, t) = \int\int p(z, y, 1; x, t)\, dz\, dy = \int \bar{p}(y; x, t)\, dy.
$$

By integrating the equations of (14) with respct to z and y, we obtain the following H57 like equation:

$$\frac{\partial n(x,t)}{\partial t} - v_{\text{hs}}(t)\frac{\partial n(x,t)}{\partial x} = (1 - n(x,t))f(x,t) - n(x,t)g(x,t),$$

where the transition rates are given by:

$$f(x,t) = \int\int k_+(z,y,x)\frac{p(z,y,0;x,t)}{1-n(x,t)}dz\,dy,$$

$$g(x,t) = \int k_-(y,x)\frac{\bar{p}(y;x,t)}{n(x,t)}dy. \tag{15}$$

We notice that this H57 version of Eq. (14) is not written in closed form, as $f(x,t)$ and $g(x,t)$ depend on the specific distribution of the degrees of freedom z and y and not only on the averaged quantity $n(x,t)$.

Recovering the H57 model. This analogy with the H57 model allows for a more direct comparison when hypotheses closer to those of the H57 model are assumed. Indeed, by canceling the degree of freedom associated with the power-stroke (i.e. $Y^t \equiv 0$), we have:

$$p(z,y,0;x,t) = \hat{p}(z;x,t)\delta(y),$$
$$\bar{p}(y;x,t) = n(x,t)\delta(y),$$

which gives, thanks to (15), $g(x,t) = k_-(0,x) = \hat{g}(x)$. Moreover, coherently with H57, let us assume that the binding rate is independent of Z^t, that is $k_+(z,0,x) = \hat{f}(x)$, which gives, thanks to (15), $f(x,t) = \hat{f}(x)$. In this way, in Caruel, Moreau, and Chapelle 2019, the authors recovered the original H57 model.

Thermal equilibrium model. More interestingly, the authors recovered an analogy with the H57 model under the hypothesis that the time scale of the macroscopic behavior is large enough for the internal degrees of freedom to be at thermal equilibrium. The equilibrium distributions can be multiplicatively decomposed as:

$$p(z,y,0;x,t) = p_0^{th}(z,y)(1 - n(x,t)),$$
$$\bar{p}(y;x,t) = p_1^{th}(y;x)n(x,t),$$

where

$$p_0^{th}(z,y) = \frac{\exp\left(-\frac{w_0(z,y)}{k_B T}\right)}{\int\int \exp\left(-\frac{w_0(z,y)}{k_B T}\right)dz\,dy},$$

$$p_1^{th}(y;x) = \frac{\exp\left(-\frac{w_1(x,y)}{k_B T}\right)}{\int \exp\left(-\frac{w_1(x,y)}{k_B T}\right)dy}.$$

When the probability distribution takes this form, Eq. (15) reduces to:

$$f(x,t) = f^{th}(x) = \int\int k_+(z,y,x)p_0^{th}(z,y)dz\,dy,$$

$$g(x,t) = g^{th}(x) = \int k_-(y,x)p_1^{th}(y;x)dy, \tag{16}$$

which gives a model, equivalent to the H57 one, in closed form. This conclusion is more than a mere analogy and it allows to shed a new light on the H57 model. The H57 model, which does not explicitly represent the power-stroke, can indeed be interpreted as a model where the variable describing the degree of freedom associated with the power-stroke is considered at equilibrium. Unlike in the H57 original formulation, where the power-stroke is simply neglected, here it is accounted for in the definition of the transition rates given by (16). This allows to relate a microscopic description of the contractile mechanism with macroscopic effective quantities.

4 Parameters estimation in H57-like models

In Sec. 3 we reviewed several models proposed in literature to describe the dynamics of force generation in the cardiac muscle tissue. Those models feature different levels of biophysical detail in the description of the complex mechanisms that determine active force generation. We have shown how the most detailed models are able to capture phenomena that cannot be captured by the simpler models, such as the fast time scale response of the muscle tissue.

However, when used in specific settings such as that of multiscale cardiac simulations (see e.g. Quarteroni et al. 2019; Salvador, Dedè, and Quarteroni 2019; Regazzoni 2019), the most detailed models are not necessarily the most suitable to apply. Indeed, some features such as the separation between the phase 1 and phase 2 of fast response (see Sec. 2.3) cannot be appreciated when the involved time scales are those characterizing the muscle movements during an heartbeat (as we will quantitatively assess later in this section). Moreover, the more detailed a model is, the more numerous parameters need to be calibrated. Because of the difficulty to measure the parameters characterizing the microscopic features of the contractile apparatus, simpler models with fewer parameters (that can be easily calibrated by macroscale measurements) are to be preferred. As a matter of fact, the best compromise between biophysical detail of the model and identifiability of its parameters ought be pursued, by "making things as simple as possible, but not simpler", to paraphrase a celebrated quote attributed to A. Einstein.

Motivated by the above observations, in this section we consider a (generalized) version of the H57 model, to investigate to which extent this model can explain the experimentally observed behaviors linked to the XB dynamics and, at the same time, how the associated parameters can be calibrated by measurements typically available from experiments.

4.1 A generalized H57 model

The H57 model is derived under the condition of full activation of the thin filament. To take into account, in a simple way, the fact that not all the regulatory units may be in permissive state (and, thus, the binding sites may not be available for XB formation), we consider two options. The first one is to multiply, in the computation of force, the number of XBs by the fraction of permissive BSs, P. The second is to replace in (4) the term $(1 - n(x,t))$ by $(P - n(x,t))$, similarly to what proposed, to account for the filaments overlapping, in Chapelle et al. 2012. Notice that, thanks to the linearity of the equation, both approaches lead to the same result. Even if this approach is approximate, as it does not take into account the possible time dependence of $P(t)$, we restrict ourselves to the condition of constant activation.

Hence, we consider the following modified H57 model, where we allow (as in Bestel, Clément, and Sorine 2001; Chapelle et al. 2012) for a dependency of the transition rate on the shortening velocity $v_{\mathrm{hs}}(t)$, and we introduce the dependence on the permissivity P:

$$\frac{\partial n(x,t)}{\partial t} - v_{\mathrm{hs}}(t)\frac{\partial n(x,t)}{\partial x} = (P - n(x,t))f(x,v(t)) - n(x,t)g(x,v(t)), \quad x \in \mathbb{R}, \, t \geq 0, \tag{17}$$

where we prefer to express the transition rates in function of the normalized shortening velocity $v(t) = v_{\mathrm{hs}}(t)/(SL_0/2)$. The force generated by half filament, by assuming that a XB attached with displacement x exerts a force of $F_{\mathrm{XB}}(x)$, is given by:

$$F_{\mathrm{hf}}(t) = \rho_{\mathrm{AM}}\int_{-\infty}^{+\infty} F_{\mathrm{XB}}(x)n(x,t)dx. \tag{18}$$

In particular, with a linear spring XB model (i.e. $F_{\mathrm{XB}}(x) = k_{\mathrm{XB}}\,x$), we have:

$$F_{\mathrm{hf}}(t) = \rho_{\mathrm{AM}}k_{\mathrm{XB}}\int_{-\infty}^{+\infty} x\,n(x,t)dx. \tag{19}$$

The macroscopic tension, in turn, is proportional to the force generated by half filament.

In (17), the quantities to be modeled (that is the "parameters" of the model) are $f(x,v)$ and $g(x,v)$. Clearly, without a detailed microscopic model of the attachment-detachment process, the two functions $f(x,v)$ and $g(x,v)$ cannot be easily calibrated from macroscale experiments.

4.2 Distribution-moments equation

Under the hypothesis that the total transition rate is independent of x (i.e. there exists a function $r(v) = f(x,v) + g(x,v)$), it is possible to write the distribution-moments equations (see Sec. 3.2). With this aim, we introduce the moments for $p \in \mathbb{N}$ (we notice that, differently from the notation used in Sec. 3.2, μ^p are dimensionless, while μ_f^p are inverse of time units):

$$\begin{aligned}
\mu^p(t) &:= \int_{-\infty}^{+\infty}\left(\frac{x}{SL_0/2}\right)^p n(x,t)\frac{dx}{D_M}, \\
\mu_f^p(v) &:= \int_{-\infty}^{+\infty}\left(\frac{x}{SL_0/2}\right)^p f(x,v)\frac{dx}{D_M}.
\end{aligned} \tag{20}$$

Thanks to this definition, $\mu^0(t)$ can be interpreted as the fraction of BSs involved in a XB. Moreover, $\mu^1(t)/\mu^0(t)$ corresponds to the average distortion of attached XBs, normalized with respect to $SL_0/2$. We notice that, under the linear spring hypothesis, thanks to Eq. (19), the total active tension is proportional to $\mu^1(t)$. Therefore, we can write $T_{\mathrm{a}}(t) = a_{\mathrm{XB}}\mu^1(t)$, where a_{XB} has the dimension of a pressure.

By multiplying by $(x/(SL_0/2))^p$, integrating over $x \in (-\infty,+\infty)$ and using the fact that $n(-\infty,t) = n(+\infty,t) = 0$, we get the following distribution-moments equations:

$$\begin{cases}
\dfrac{d}{dt}\mu^0(t) = -r(v(t))\mu^0(t) + P\,\mu_f^0(v(t)) & t \geq 0, \\[2mm]
\dfrac{d}{dt}\mu^1(t) = -r(v(t))\mu^1(t) + P\,\mu_f^1(v(t)) - \mu^0(t)v(t) & t \geq 0.
\end{cases} \tag{21}$$

17

By assuming that $f + g$ is independent of x, the freedom in the choice of the functions describing the model has been reduced, as we have to model $\mu_f^0(v)$, $\mu_f^1(v)$ and $r(v)$, that are only functions of v.

4.3 Steady-state solution

By assuming a constant shortening $v(t) \equiv \bar{v}$, and solving (20) by setting all time derivatives equal to zero, we get the following steady-state solution:

$$
\begin{aligned}
\bar{\mu}^0 &= P \frac{\mu_f^0(\bar{v})}{r(\bar{v})}, \\
\bar{\mu}^1 &= P \frac{\mu_f^1(\bar{v}) - \mu^0(t)\bar{v}}{r(\bar{v})} = P \left(\frac{\mu_f^1(\bar{v})}{r(\bar{v})} - \frac{\mu_f^0(\bar{v})}{r(\bar{v})^2} \bar{v} \right).
\end{aligned}
\tag{22}
$$

Since the force is proportional to μ^1, the last equation gives the force-velocity relationship. Moreover, the steady-state solution of Eq. (22) allows to compute some quantities of interest. The force in isometric conditions is given by $T_a^{\text{iso}} = a_{\text{XB}}(\bar{\mu}^1)_{\bar{v}=0} = a_{\text{XB}} P \mu_f^1(0)/r(0)$. The fraction of attached XBs, in turn, is given by $(\bar{\mu}^0)_{\bar{v}=0} = P \mu_f^0(0)/r(0)$. Finally, the maximum shortening velocity v^{max} can be computed as the positive solution of the equation $\mu_f^1(v^{\text{max}})r(v^{\text{max}}) = \mu_f^0(v^{\text{max}})v^{\text{max}}$.

As a matter of fact, the above mentioned quantities take special forms under more restrictive hypotheses for f and g. For instance, it is reasonable to assume that the sliding velocity only affects the detachment rate, so that $f(x, v) = \bar{f}(x)$. In this case, assuming again that the sum $f + g$ is independent of x, we can write $g(x, v) = r_0 - \bar{f}(x) + q(v)$, for some $q(v)$ such that $q(0) = 0$ and where $r_0 = r(0)$. The term $q(v)$ models the rate of XB destruction due to rapid length changes. Under this additional hypothesis, the objects to be modeled are just $\mu_{\bar{f}}^0$, $\mu_{\bar{f}}^1$, r_0 and $q(v)$ (three scalar values and a function). If we set, as in Chapelle et al. 2012, $q(v) = \alpha|v|$ (which reduces the quantities to be modeled to 4 scalars), the maximum shortening velocity takes the form:

$$
v^{\text{max}} = r_0 \left(\frac{\mu_{\bar{f}}^0}{\mu_{\bar{f}}^1} - \alpha \right)^{-1}.
$$

Let us consider now the particular case of constant attachment rate within the interval $x \in [s_0, s_0 + h]$ (as in Bestel, Clément, and Sorine 2001):

$$
f(x, v) = k_{\text{ATP}} \mathbb{1}_{[s_0, s_0 + h]}(x), \qquad g(x, v) = k_{\text{ATP}}(1 - \mathbb{1}_{[s_0, s_0 + h]}(x)) + q(v). \tag{23}
$$

This choice falls within the above mentioned case. The quantities to be modeled, in this case, are k_{ATP}, h, s_0, $q(v)$, which are linked to the previous ones by:

$$
\mu_{\bar{f}}^0 = k_{\text{ATP}} \frac{h}{D_M}, \qquad \mu_{\bar{f}}^1 = k_{\text{ATP}} \frac{h(h + 2\, s_0)}{SL_0\, D_M}, \qquad r_0 = k_{\text{ATP}}, \tag{24}
$$

and, conversely:

$$
h = \frac{k_{\text{ATP}}}{\mu_{\bar{f}}^0 D_M}, \qquad s_0 = \frac{1}{2} \left(\frac{SL_0\, D_M \mu_{\bar{f}}^1}{k_{\text{ATP}} h} - h \right), \qquad k_{\text{ATP}} = r_0, \tag{25}
$$

which allows to give a microscopical interpretation to the constants. In this case, the steady-state solution reads:

$$\bar{\mu}^0 = P \frac{h}{D_M} \left(1 + \frac{q(\bar{v})}{k_{\text{ATP}}} \right)^{-1},$$

$$\bar{\mu}^1 = P \frac{h}{2\,D_M} \left(1 + \frac{q(\bar{v})}{k_{\text{ATP}}} \right)^{-2} \left(\frac{h+2s_0}{SL_0/2} \left(1 + \frac{q(\bar{v})}{k_{\text{ATP}}} \right) - 2\frac{\bar{v}}{k_{\text{ATP}}} \right). \tag{26}$$

Moreover, the isometric tension is given by $T_{\text{a}}^{\text{iso}} = a_{\text{XB}} P \frac{h(h+2\,s_0)}{SL_0\,D_M}$ and the fraction of attached XBs in isometric conditions is $(\bar{\mu}^0)_{\bar{v}=0} = P\frac{h}{D_M}$. With the choice $q(v) = \alpha|v|$, the maximum shortening velocity, if $\alpha < \frac{SL_0}{h+2s_0}$, is given by:

$$v^{\max} = k_{\text{ATP}} \left(\frac{SL_0}{h + 2s_0} - \alpha \right)^{-1}.$$

Conversely, if $\alpha \geq \frac{SL_0}{h+2s_0}$, $v^{\max}$ is not defined, as the force-velocity relationship never intercepts the $T_{\text{a}} = 0$ axis.

4.4   Fast transients solution

Because of the lack of explicit representation of the power-stroke, the generalized H57 model (20) fails to reproduce the three different phases after a fast step, either in length or in tension (see Sec. 2.3). Indeed, in place of the two fast steps (the elastic response and the fast force recovery, due to the power-stroke), we have only a single fast step, followed by the slow force recovery (or by the constant shortening, in the case of the soft device experiment). In this section, we study the predictions of the model concerning such fast phase.

In order to study the behavior predicted by the model when a fast transient experiment is performed (here we focus on steps in length), we suppose that at $t = 0$ the muscle is in steady-state isometric conditions (i.e. $\mu^0(0) = P\mu_f^0(0)/r(0)$, $\mu^1(0) = P\mu_f^1(0)/r(0)$). We then consider a sudden change in length ΔL (the relative shortening w.r.t. half sarcomere, thus a dimensionless quantity), accomplished in a small amount of time δ (i.e. $v(t) = \frac{\Delta L}{\delta}\mathbb{1}_{[0,\delta]}(t)$). We study the solution at $t = \delta$, for $\delta \to 0^+$.

The solution of (21), when $v(t) = \bar{v}$ is constant, is given by:

$$\begin{cases} \mu^0(t) = \mu^0(0) + \left(P\frac{\mu_f^0(\bar{v})}{r(\bar{v})} - \mu^0(0) \right) \left(1 - e^{-r(\bar{v})t} \right) & t \geq 0, \\[2ex] \mu^1(t) = \mu^1(0) + \left(P\left(\frac{\mu_f^1(\bar{v})}{r(\bar{v})} - \frac{\mu_f^0(\bar{v})}{r(\bar{v})^2}\bar{v} \right) - \mu^1(0) \right) \left(1 - e^{-r(\bar{v})t} \right) & \\[2ex] \quad + \left(P\frac{\mu_f^0(\bar{v})}{r(\bar{v})} - \mu^0(0) \right) \bar{v}\,t\,e^{-r(\bar{v})t} & t \geq 0. \end{cases} \tag{27}$$

By setting $\bar{v} = \frac{\Delta L}{\delta}$, the tension at the end of the length step reads:

$$T_{\text{a}}(\delta) = a_{\text{XB}}\mu^1(\delta) = a_{\text{XB}} P \left[\frac{\mu_f^1}{r(0)} + \left(\mu_f^1\left(\frac{1}{r(\bar{v})} - \frac{1}{r(0)} \right) - \frac{\mu_f^0}{r(\bar{v})^2}\frac{\Delta L}{\delta} \right) \right.$$

$$\left. \left(1 - e^{-r(\bar{v})\delta} \right) + \mu_f^0 \left(\frac{1}{r(\bar{v})} - \frac{1}{r(0)} \right) \Delta L\,e^{-r(\bar{v})\delta} \right]. \tag{28}$$

For time $t > \delta$, the solution is given by (27), shifted by δ, with $\bar{v} = 0$ and with initial state given by (28). However, to characterize the fast phase, we are here only interested in studying the asymptotic behavior of (28) for $\delta \to 0^+$. The solution depends on the behavior of $r(v)$ for $v \to +\infty$. We distinguish between four possible cases: bounded or with sublinear, linear or superlinear growth.

- **Saturating behavior.** Suppose that for $v \to +\infty$, $r(v) \to r_{\max}$. Then, we have:

$$
\begin{aligned}
T_{\mathrm{a}}(\delta) &\sim a_{\mathrm{XB}}P\left[\frac{\mu_f^1}{r(0)} + \frac{\mu_f^0}{r_{\max}}\Delta L - \mu_f^0\left(\frac{1}{r_{\max}} - \frac{1}{r(0)}\right)\Delta L\right] \\
&= \frac{a_{\mathrm{XB}}P\mu_f^1}{r(0)} - \frac{a_{\mathrm{XB}}P\mu_f^0}{r(0)}\Delta L,
\end{aligned}
\tag{29}
$$

which is a linear response, with slope $\frac{a_{\mathrm{XB}}P\mu_f^0}{r(0)}$. In this case, therefore, the fast response is that of a linear elastic spring (like the T_1-L_1 curve), with stiffness given by $\frac{a_{\mathrm{XB}}P\mu_f^0}{r(0)}$.

- **Sublinear growth.** Suppose that $r(v) \to +\infty$, but $r(v)/v \to 0$. Then we have $r(\bar{v})\delta = r(\frac{\Delta L}{\delta})\delta \to 0$, and thus:

$$
T_{\mathrm{a}}(\delta) \sim \frac{a_{\mathrm{XB}}P\mu_f^1}{r(0)} - \frac{a_{\mathrm{XB}}P\mu_f^0}{r(0)}\Delta L,
\tag{30}
$$

which is the same behavior as the previous case. For this reason, from now on, we will include both cases in the sublinear growth one.

- **Linear growth.** Suppose now that $r(v) \sim \alpha v$. In this case, we have $r(\bar{v})\delta = r(\frac{\Delta L}{\delta})\delta \sim \alpha \Delta L$ and thus:

$$
T_{\mathrm{a}}(\delta) \sim \frac{a_{\mathrm{XB}}P\mu_f^1}{r(0)}e^{-\alpha\Delta L} - \frac{a_{\mathrm{XB}}P\mu_f^0}{r(0)}e^{-\alpha\Delta L}\Delta L.
\tag{31}
$$

Hence, in this case the response is different from a linearly elastic element. In order to compare the stiffness for small step lengths with the stiffness predicted in the sublinear growth case, we linearize around $\Delta L = 0$, getting:

$$
T_{\mathrm{a}}(\delta) \sim \frac{a_{\mathrm{XB}}P\mu_f^1}{r(0)} - a_{\mathrm{XB}}P\frac{\mu_f^0 + \alpha\mu_f^1}{r(0)}\Delta L.
\tag{32}
$$

In conclusion, the stiffness associated with small steps is increased by a term $\alpha\, a_{\mathrm{XB}}\, P\, \mu_f^1/r(0)$.

- **Superlinear growth.** Suppose that $r(v) \to +\infty$ and $r(v)/v \to +\infty$. Then we have $r(\bar{v})\delta = r(\frac{\Delta L}{\delta})\delta \to +\infty$, which gives:

$$
T_{\mathrm{a}}(\delta) \to 0.
\tag{33}
$$

This means that, if the destruction rate grows more than linearly in the velocity, then, in the limit of an instantaneous length step, the velocity is such that all the XB are destroyed.

4.5 Parameters calibration

As noticed in Sec. 4, the calibration of the generalized H57 model (20) requires the definition of the functions $f(x, v)$ and $g(x, v)$. However, such functions, without a detailed microscopical model, are difficult to be determined solely based on experimental results. By assuming that the sum $f + g$ is independent of x and that v only affects detachment, instead, the objects to be estimated reduce to the four scalars $\mu_{\bar{f}}^0$, $\mu_{\bar{f}}^1$, r_0, a_{XB} and the function $q(v)$. In addition, as shown in Sec. 4.4, the response to fast transients is only affected by the asymptotic behavior of $q(v)$ for $|v| \to +\infty$, while the force-velocity relationship is only affected by the values of $q(v)$ for $0 \leq v \leq v^{\max}$. Therefore, in the following, we will restrict ourselves to the following two cases:

- **Sublinear growth**: we consider $q(v)$ such that $q(v) = \alpha|v|$ for small velocities, while for $|v| \to +\infty$ we have $q(v)/|v| \to 0$.

- **Linear growth**: we consider for simplicity the case $q(v) = \alpha|v|$.

We do not consider the case of superlinear growth since in the limit of instantaneous response it predicts the detachment of all the XBs, which hinders the possibility of fitting any fast response curve.

The behavior of the model is thus determined by five scalar parameters ($\mu_{\bar{f}}^0$, $\mu_{\bar{f}}^1$, r_0, a_{XB}, α) and by the asymptotic of behavior $q(v)$ (linear or sublinear). From the previous sections, it follows that by acting on the above mentioned parameters, the generalized H57 model can match the following experimentally measured quantities.

- Under **isometric conditions**, the solution allows to compute the following quantities.

  ○ The isometric tension:

  $$T_{\mathrm{a}}^{\mathrm{iso}} = a_{\mathrm{XB}}(\bar{\mu}^1)_{\bar{v}=0} = a_{\mathrm{XB}} P \frac{\mu_{\bar{f}}^1}{r_0}.$$

  ○ The fraction of attached XBs:

  $$\mu_{\mathrm{iso}}^0 := (\bar{\mu}^0)_{\bar{v}=0} = P \frac{\mu_{\bar{f}}^0}{r_0}.$$

- The **force-velocity** is invariant after normalization with respect to the isometric tension (see 2.2). The generalized H57 model correctly predicts this fact. If we suppose, for instance, to vary the calcium concentration and consequently the value of P, the normalized force-length relationship would be unaffected. Indeed, the normalized force-length relationship is given by:

  $$T_{\mathrm{a}}/T_{\mathrm{a}}^{\mathrm{iso}} = \frac{1}{1 + \alpha \frac{|v|}{r_0}} - \frac{\mu_{\bar{f}}^0/\mu_{\bar{f}}^1}{\left(1 + \alpha \frac{|v|}{r_0}\right)^2} \frac{v}{r_0}.$$

  Unlike the original H57 model, that predicts a linear force-velocity relationship (corresponding to the case $\alpha = 0$), by allowing for a dependence of the detachment rate on the velocity, the experimentally observed convex shape can be obtained. Indeed, by properly choosing the parameters of the model, one can fit the following two quantities, characterizing the relationship for large and for small velocities, respectively.

○ The maximum shortening velocity:

$$v^{\mathrm{max}} = r_0 \left(\frac{\mu_{\bar{f}}^0}{\mu_{\bar{f}}^1} - \alpha \right)^{-1}.$$

○ The inverse of the sensitivity of the normalized force w.r.t. velocity changes in isometric conditions (whose interpretation in the force-velocity curve is shown in Fig. 7a):

$$v^0 := - \left(\frac{\partial \bar{T}_{\mathrm{a}}/T_{\mathrm{a}}^{\mathrm{iso}}}{\partial v} |_{v=0} \right)^{-1} = r_0 \left(\frac{\mu_{\bar{f}}^0}{\mu_{\bar{f}}^1} + \alpha \right)^{-1}.$$

With the original H57 model, having $\alpha = 0$, we have $v^{\mathrm{max}} = v^0$ and the behaviors at small and large velocities cannot be decoupled.

- The **fast transients** response is characterized by two distinct curves, associated with different time scales (see Sec. 2.3). As previously noticed, models belonging to the H57 class do not incorporate a description of the power-stroke and are thus only capable of reproducing the instantaneous linear response. However, if we interpret the H57 model as the limit of a more detailed model where the power-stroke is considered at equilibrium (see Sec. 3.3.2), the fast response is only characterized by a single time constant, corresponding to the slowest of the two time constants observed experimentally. Such time constant, therefore, corresponds to the second of the phases considered in 2.3. For this reason, we interpret the stiffness associated with fast steps in the generalized H57 model of Eq. (20) as the stiffness associated with the T_2-L_2 curve. In particular, the parameters can be chosen so that to fit the following value.

  ○ The tangent normalized stiffness in isometric conditions (see Fig. 7b):

$$\tilde{k}_2 := - \frac{\partial T_{\mathrm{a}}(0^+)/T_{\mathrm{a}}^{\mathrm{iso}}}{\partial \Delta L} |_{\Delta L=0} = \begin{cases} \mu_{\bar{f}}^0/\mu_{\bar{f}}^1 & \text{sublinear q,} \\ \mu_{\bar{f}}^0/\mu_{\bar{f}}^1 + \alpha & \text{linear q.} \end{cases}$$

Moreover, we notice that, if one is interested in macroscopic regimes characterized by sufficiently large time scales, only the region of the T_2-L_2 curve associated with small steps is of interest. Indeed, the larger the length step, the higher shortening velocities are needed to appreciate the distinction between phase 2 and phases 3-4 of the response (we will quantitatively support this point in Sec. 4.6). In conclusion, since in the region associated with small steps a linear fit provides a good approximation of the curve, the quantity $\tilde{k}_2$ alone provides a sufficiently complete characterization of the fast step response.

The five parameters characterizing the generalized H57 model (20) can be assigned to match the five measured quantities $T_{\mathrm{a}}^{\mathrm{iso}}$, μ_{iso}^0, v^{max}, v^0 and $\tilde{k}_2$. This provides a practical way of calibrating the model parameters from experimental measurements. Specifically, in the linear growth case, the parameters of the model can be determined

(a) Force-velocity relatioship   (b) Fast transient response
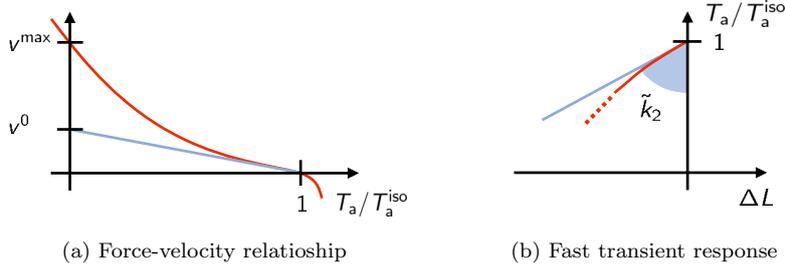
Figure 7: The force-velocity relationship (a) is characterized by the maximum shortening velocity v^{max} (the intercept of the curve with the axis $T_{\mathrm{a}} = 0$) and by the inverse sensitivity of the force to velocity in isometric conditions v^0, which can be interpreted as the intercept with the axis $T_{\mathrm{a}} = 0$ of the tangent to the curve in isometric conditions. On the other hand, the response to fast transients is characterized by the normalized stiffness $\tilde{k}_2$, where the subscript 2 reflects the fact that this value characterizes the T_2-L_2 response.

by the following relationships:

$$
\begin{aligned}
r_0 &= \tilde{k}_2\, v^0, \\
\alpha &= \frac{r_0}{2}\left((v^0)^{-1} - (v^{\mathrm{max}})^{-1}\right) = \frac{\tilde{k}_2}{2}\left(1 - \frac{v^0}{v^{\mathrm{max}}}\right), \\
\mu_{\bar{f}}^0 &= \frac{\mu_{\mathrm{iso}}^0 r_0}{P} = \frac{\mu_{\mathrm{iso}}^0 \tilde{k}_2 v^0}{P}, \\
\mu_{\bar{f}}^1 &= \left(\tilde{k}_2 - \alpha\right)^{-1} \mu_{\bar{f}}^0, \\
a_{\mathrm{XB}} &= \frac{T_{\mathrm{a}}^{\mathrm{iso}} r_0}{\mu_{\bar{f}}^1 P} = \frac{T_{\mathrm{a}}^{\mathrm{iso}} \tilde{k}_2 (1 + \frac{v^0}{v^{\mathrm{max}}})}{2\mu_{\mathrm{iso}}^0}.
\end{aligned}
\tag{34}
$$

Conversely, in the sublinear growth case we have:

$$
\begin{aligned}
r_0 &= \frac{2\, \tilde{k}_2 v^{\mathrm{max}}}{1 + v^{\mathrm{max}}/v^0}, \\
\alpha &= \frac{v^{\mathrm{max}} - v^0}{v^{\mathrm{max}} + v^0} \tilde{k}_2, \\
\mu_{\bar{f}}^0 &= \frac{\mu_{\mathrm{iso}}^0 r_0}{P}, \\
\mu_{\bar{f}}^1 &= \mu_{\bar{f}}^0 / \tilde{k}_2, \\
a_{\mathrm{XB}} &= \frac{T_{\mathrm{a}}^{\mathrm{iso}} r_0}{\mu_{\bar{f}}^1 P}.
\end{aligned}
\tag{35}
$$

In both the cases of linear and sublinear growth, P denotes the permissivity associated with the condition in which $T_{\mathrm{a}}^{\mathrm{iso}}$ and μ_{iso}^0 are measured.

Remark 1. Among the five quantities used to calibrate the model parameters, only one (namely μ_{iso}^0) is related to the microscopic scale, while the others are related to the macroscale. The measurement of μ_{iso}^0 may be hard to be accomplished, indeed.

Table 1: List of the experimental data used for model calibration.

Parameter	Value	Units	Reference
$T_\mathrm{a}^\mathrm{iso}$	120	kPa	Ter Keurs, Hollander, and Keurs 2000
μ_iso^0	0.22	-	Brunello et al. 2014
v^max	8	s^{-1}	Caremani et al. 2016
v^0	2	s^{-1}	Caremani et al. 2016
$\tilde{k}_2$	66	-	Caremani et al. 2016

Table 2: List of the calibrated parameters in the sublinear, linear and superlinear growth cases.

Parameter	Units	Sublinear growth	Linear growth	Superlinear growth
a_XB	MPa	35.46	22.16	20.46
$\mu_{\bar{f}}^1$	s^{-1}	0.7040	0.7040	0.7040
$\mu_{\bar{f}}^0$	s^{-1}	45.76	28.60	2.640
α	$-$	39.00	24.37	2.250
r_0	s^{-1}	208.0	130.0	12.00

However, if one is interested only in the prediction of the generated tension and not in the moments μ^0 and μ^1, the calibration can be accomplished regardless of μ_iso^0, by considering only the macroscopic scale. As a matter of fact, the three parameters a_XB, $\mu_{\bar{f}}^0$ and $\mu_{\bar{f}}^1$ appear always in the two combinations $a_\mathrm{XB}\mu_{\bar{f}}^1$ and $\mu_{\bar{f}}^0/\mu_{\bar{f}}^1$, apart from in the expression of μ_iso^0. Therefore, one could calibrate the two combined terms $a_\mathrm{XB}\mu_{\bar{f}}^1$ and $\mu_{\bar{f}}^0/\mu_{\bar{f}}^1$ rather than the three parameters.

In other terms, thanks to the linearity of the equations, the value of μ_iso^0 used in the calibration of the model only affects the prediction of the quantities related to the microscale (i.e. μ^0 and μ^1), but not the tension T_a. Therefore, as far as the modeling of T_a is concerned, the model is fully characterized by the four quantities $T_\mathrm{a}^\mathrm{iso}$, v^max, v^0 and $\tilde{k}_2$.

4.6   Numerical results

In this section, we perform the calibration of the parameters of the model (21), by using the relationships derived in Sec. 4.5 (Eqs. (34) and (35)), starting from experimental measurements, reported in Tab. 1, together with a reference to the source in literature. We consider data coming from intact (i.e. non skinned, see Kentish et al. 1986; Backx et al. 1995; Gao et al. 1994; Dobesh, Konhilas, and Tombe 2002) cardiac rat cell at room temperature. The unique datum not satisfying these condition is μ_iso^0 (which is acquired from skeletal frog muscle). However, as we mentioned in Sec. 4.5, the value of such parameter only affects the value of the microscopic variables (i.e. μ^p), but not the predicted active tension. In Tab. 2 we report the parameters obtained by calibrating the model in both the sublinear and linear growth cases.

In Fig. 8 we show the force-velocity relationship obtained with the calibrated model (in the linear growth case), together with the experimental data from Caremani et al. 2016. We can see that the calibration procedure is successful if matching the prediction of the model with the experimental measurements.
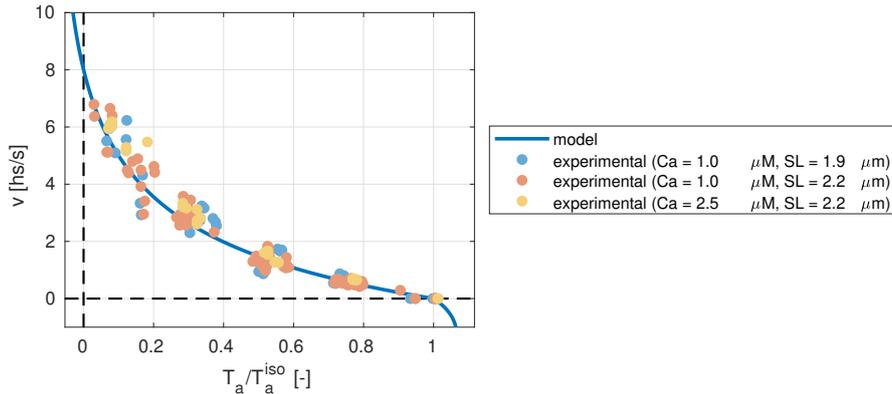
Figure 8: Force-velocity relationship obtained with the model (21), compared with experimental data from Caremani et al. 2016.

Then, in Fig. 9 we consider the fast response predicted by the model. With this aim, we let the model reach the steady state and then we apply a length step, by applying a constant velocity in a small time interval Δt. Finally, we plot the tension obtained at the end of the step against the step length ΔL. We repeat this protocol twice: first, by reproducing the same conditions employed in laboratory, that is by applying the length step in a very small time interval ($\Delta t = 200\,\mu s$, see Caremani et al. 2016 and Sec. 2.3); then, we repeat the simulation, this time by applying the step with a lower shortening velocity, compatible with the typical velocity by which the cardiac tissue shortens during an heartbeat (we set $v = 0.5\,s^{-1}$).

We show in Figs. 9a and 9b the results obtained, in the case of sublinear (by setting $q(v) = \alpha\sqrt{|v|}$) and linear (by setting $q(v) = \alpha|v|$) growth of q, respectively. The models here considered do not explicitly represent the power-stroke, whose effect is instead accounted for in the definition of the attachment-detachment rates (see Sec. 4.5). Therefore, we compare the tension after the $200\,\mu s$ fast transient with the T_2-L_2 data, experimentally measured by applying a fast step within the same time interval (see again Sec. 4.5). The good match between the simulation results and the experimental measurements provide a further validation of the calibration procedure.

The curves obtained by letting the tissue shorten with a velocity similar to that observed during an heartbeat are close to those obtained with an almost instantaneous step, for small values of ΔL. Conversely, for larger ΔL, the former curves saturate and a smaller force drop is observed. The reason is that a large length step takes a longer time to be accomplished, and, consequently, the time interval is large enough for the attachment-detachment process to partially recover the original tension. In other terms, when we consider the typical time scales of an heartbeat, the dynamics of the length changes is not sufficiently fast to appreciate the scale separation between the different phases following a fast transient (see Sec. 2.3). This provides a justification for the fact that a lumped description of the power-stroke is an acceptable approximation if the model is used for organ-level simulations and for the fact that, in the model calibration, fitting the T_2-L_2 curve for small values of ΔL is sufficient (see Sec. 4.5).

Finally, in Fig. 9c we show the fast-transient obtained in the case of superlinear growth of r (by setting $q(v) = \alpha(|v| + v^2)$). In this case, since we de not have a relationship equivalent to (Eqs. (34) and (35)), we employ the relationship derived in the linear growth case, by adjusting the parameter $\tilde{k}_2$ to fit the experimental data.
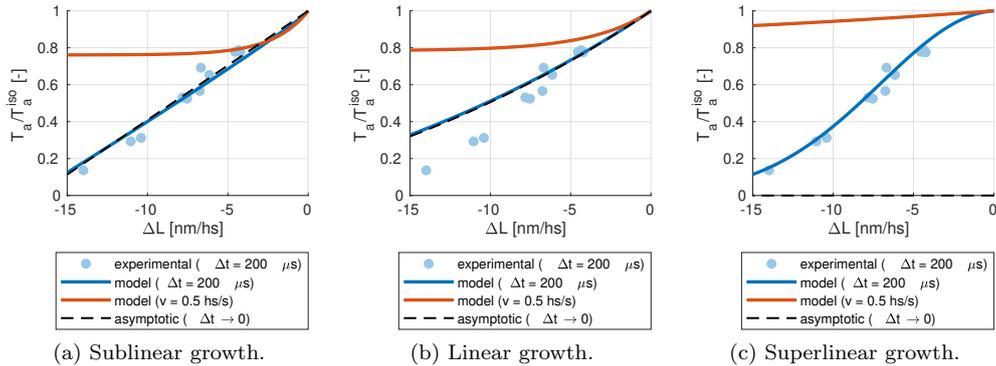
Figure 9: Normalized force after the application of a fast length step ΔL. The fast steps reported by the blue lines (model result) and the blue circles (T_2-L_2 experimental data from Caremani et al. 2016) are applied within a time interval of $\Delta t = 200\,\mu s$, while the red lines refer to fast steps applied with a shortening velocity of $v = 0.5\,s^{-1}$. Finally, the black dashed lines refer to the asymptotical response for $\Delta t \to 0$.

We notice that, even if the asymptotic analysis of Sec. 4.4 shows that, in the limit of $v \to \infty$, the response to fast steps leads to vanishing tension, when the step is applied with a finite time interval, we obtain a curve that is in agreement with the experimental measurements.

5   Conclusions

In this paper we reviewed several models describing the interaction between actin and myosin in cardiac muscle cells. As a matter of fact, different models, with different degrees of biophysical detail, are available in literature. The most detailed models are able of capturing phenomena, such as the response to fast steps, occurring at the fastest time scales involved in the force generation mechanism (Marcucci and Truskinovsky 2010b; Marcucci and Truskinovsky 2010a; Caruel, Moireau, and Chapelle 2019). Conversely, the models belonging to the family of the H57 model, while being able of reproducing the phenomena occurring at slower time scales (such as the force-velocity relationship), do not allow to match the two different experimentally observed fast responses exhibited by the muscle tissue when a step (either in length or in tension) is applied.

In Caruel, Moireau, and Chapelle 2019 the authors show that, if the considered time scales are large enough for the variable describing the power-stroke to be considered at thermal equilibrium, detailed soft-spring models that explicitly represent the power-stroke are formally recast to the H57 model. Motivated by this observation, we have investigated the capabilities of a modified version of the H57 model to reproduce the experimentally observed characterizations of the force generation phenomenon. Such model, compared to the most detailed models that explicitly represent the power-stroke, has the significant advantage of featuring only four independent parameters, that can be determined starting from macroscopic measurements typically available from experiments. In particular, the model can match the isometric active tension, the force-velocity relationship and the stiffness associated to small steps. Hence, if the characteristic time scales of the phenomena under exam are slower than

the fast time scale of the power stroke (such as in full-organ cardiac simulations), the models of the H57 family match a good balance between model accuracy and parameters identifiability.

Acknowledgements

References

Aliev, R. R. and A. V. Panfilov (1996). "A simple two-variable model of cardiac excitation". In: *Chaos, Solitons & Fractals* 7.3, pp. 293–301.

Backx, P., W. Gao, M. Azan-Backx, and E. Marbán (1995). "The relationship between contractile force and intracellular [Ca2+] in intact rat cardiac trabeculae." In: *The Journal of General Physiology* 105.1, pp. 1–19.

Bers, D. (2001). *Excitation-contraction coupling and cardiac contractile force*. Vol. 237. Springer Science & Business Media.

Bestel, J., F. Clément, and M. Sorine (2001). "A biomechanical model of muscle contraction". In: *International Conference on Medical Image Computing and Computer-Assisted Intervention*. Springer, pp. 1159–1161.

Brokaw, C. (1976). "Computer simulation of flagellar movement. IV. Properties of an oscillatory two-state cross-bridge model". In: *Biophysical Journal* 16.9, pp. 1029–1041.

Brunello, E., M. Caremani, L. Melli, M. Linari, M. Fernandez-Martinez, T. Narayanan, M. Irving, G. Piazzesi, V. Lombardi, and M. Reconditi (2014). "The contributions of filaments and cross-bridges to sarcomere compliance in skeletal muscle". In: *The Journal of Physiology* 592.17, pp. 3881–3899.

Bueno-Orovio, A., E. M. Cherry, and F. H. Fenton (2008). "Minimal model for human ventricular action potentials in tissue". In: *Journal of Theoretical Biology* 253.3, pp. 544–560.

Caremani, M., F. Pinzauti, M. Reconditi, G. Piazzesi, G. J. Stienen, V. Lombardi, and M. Linari (2016). "Size and speed of the working stroke of cardiac myosin in situ". In: *Proceedings of the National Academy of Sciences* 113.13, pp. 3675–3680.

Caruel, M. (2011). "Mechanics of Fast Force Recovery in striated muscles". PhD thesis. Ecole Polytechnique.

Caruel, M., P. Moireau, and D. Chapelle (2019). "Stochastic modeling of chemical–mechanical coupling in striated muscles". In: *Biomechanics and Modeling in Mechanobiology* 18.3, pp. 563–587.

Caruel, M. and L. Truskinovsky (2018). "Physics of muscle contraction". In: *Reports on Progress in Physics* 81.3, p. 036602.

Chabiniok, R., V. Wang, M. Hadjicharalambous, L. Asner, J. Lee, M. Sermesant, E. Kuhl, A. Young, P. Moireau, M. Nash, D. Chapelle, and D. Nordsletten (2016). "Multiphysics and multiscale modelling, data–model fusion and integration of organ physiology in the clinic: ventricular cardiac mechanics". In: *Interface Focus* 6.2, p. 20150083.

Chapelle, D., P. Le Tallec, P. Moireau, and M. Sorine (2012). "Energy-preserving muscle tissue model: formulation and compatible discretizations". In: *International Journal for Multiscale Computational Engineering* 10.2.

Colli Franzone, P, L. F. Pavarino, and G. Savaré (2006). "Computational electrocardiology: mathematical and numerical modeling". In: *Complex Systems in Biomedicine*. Springer, pp. 187–241.

Colli Franzone, P., L. F. Pavarino, and S. Scacchi (2014). *Mathematical cardiac electrophysiology*. Vol. 13. Springer.

Crampin, E. J., M. Halstead, P. Hunter, P. Nielsen, D. Noble, N. Smith, and M. Tawhai (2004). "Computational physiology and the physiome project". In: *Experimental Physiology* 89.1, pp. 1–26.

Dobesh, D., J. Konhilas, and P. de Tombe (2002). "Cooperative activation in cardiac muscle: impact of sarcomere length". In: *American Journal of Physiology-Heart and Circulatory Physiology* 51.3, H1055.

Fink, M., S. Niederer, E. Cherry, F. Fenton, J. Koivumäki, G. Seemann, R. Thul, H. Zhang, F. Sachse, D. Beard, E. Crampin, and N. Smith (2011). "Cardiac cell modelling: observations from the heart of the cardiac physiome project". In: *Progress in Biophysics and Molecular Biology* 104.1, pp. 2–21.

Gao, W., P. Backx, M. Azan-Backx, and E. Marban (1994). "Myofilament Ca2+ sensitivity in intact versus skinned rat ventricular muscle." In: *Circulation Research* 74.3, pp. 408–415.

Gerbi, A., L. Dedè, and A. Quarteroni (2018). "A monolithic algorithm for the simulation of cardiac electromechanics in the human left ventricle". In: *Mathematics in Engineering* 1.1, pp. 1–37.

Gordon, A., A. F. Huxley, and F. Julian (1966). "The variation in isometric tension with sarcomere length in vertebrate muscle fibres". In: *The Journal of Physiology* 184.1, pp. 170–192.

Guccione, J. M., A. D. McCulloch, and L. Waldman (1991). "Passive material properties of intact ventricular myocardium determined from a cylindrical model". In: *Journal of Biomechanical Engineering* 113.1, pp. 42–55.

Hill, A. (1938). "The heat of shortening and the dynamic constants of muscle". In: *Proceedings of the Royal Society of London B: Biological Sciences* 126.843, pp. 136–195.

Hodgkin, A. L. and A. F. Huxley (1952). "A quantitative description of membrane current and its application to conduction and excitation in nerve". In: *The Journal of Physiology* 117.4, pp. 500–544.

Holzapfel, G. A. and R. W. Ogden (2009). "Constitutive modelling of passive myocardium: a structurally based framework for material characterization". In: *Philosophical Transactions of the Royal Society A: Mathematical, Physical and Engineering Sciences* 367.1902, pp. 3445–3475.

Hunter, P., A. McCulloch, and H. Ter Keurs (1998). "Modelling the mechanical properties of cardiac muscle". In: *Progress in Biophysics and Molecular Biology* 69.2, pp. 289–331.

Hussan, J., P. de Tombe, and J. Rice (2006). "A spatially detailed myofilament model as a basis for large-scale biological simulations". In: *IBM Journal of Research and Development* 50.6, pp. 583–600.

Huxley, A. and R. Simmons (1971). "Proposed mechanism of force generation in striated muscle". In: *Nature* 233.5321, pp. 533–538.

Huxley, A. F. (1957). "Muscle structure and theories of contraction". In: *Progress in Biophysics and Biophysical Chemistry* 7, pp. 255–318.

Jenkins, G. W., C. P. Kemnitz, and G. J. Tortora (2007). *Anatomy and physiology: from science to life*. Wiley Hoboken.

Karatzas, I. and S. E. Shreve (1998). *Brownian Motion and Stochastic Calculus*. Springer.

Katz, A. M. (2010). *Physiology of the Heart*. Lippincott Williams & Wilkins.

Keener, J. and J. Sneyd (2009). *Mathematical Physiology*. Vol. 1. Springer.

Kentish, J., H. ter Keurs, L. Ricciardi, J. Bucx, and M. Noble (1986). "Comparison between the sarcomere length-force relations of intact and skinned trabeculae from rat right ventricle. Influence of calcium concentrations on these relations." In: *Circulation Research* 58.6, pp. 755–768.

Kimmig, F. (2019). "Multi-scale modeling of muscle contraction - From stochastic dynamics of molecular motors to continuum mechanics". PhD thesis. Université Paris-Saclay.

Kimmig, F., M. Caruel, P. Moreau, and D. Chapelle (2019). "Activation-contraction coupling in a multiscale heart model". In: *Proceedings of CMBE 2019 (volume 1)*, pp. 96–99.

Land, S., S. A. Niederer, J. M. Aronsen, E. K. Espe, L. Zhang, W. E. Louch, I. Sjaastad, O. M. Sejersted, and N. P. Smith (2012). "An analysis of deformation-dependent electromechanical coupling in the mouse heart". In: *The Journal of Physiology* 590.18, pp. 4553–4569.

Lymn, R. and E. W. Taylor (1971). "Mechanism of adenosine triphosphate hydrolysis by actomyosin". In: *Biochemistry* 10.25, pp. 4617–4624.

Marcucci, L. and L. Truskinovsky (2010a). "Mechanics of the power stroke in myosin II". In: *Physical Review E* 81.5, p. 051915.

— (2010b). "Muscle contraction: A mechanical perspective". In: *The European Physical Journal E* 32.4, pp. 411–418.

Murray, C. J., K. F. Ortblad, C. Guinovart, S. S. Lim, T. M. Wolock, D. A. Roberts, E. A. Dansereau, N. Graetz, R. M. Barber, J. C. Brown, et al. (2014). "Global, regional, and national incidence and mortality for HIV, tuberculosis, and malaria during 1990–2013: a systematic analysis for the Global Burden of Disease Study 2013". In: *The Lancet* 384.9947, pp. 1005–1070.

Niederer, S. A., P. J. Hunter, and N. P. Smith (2006). "A quantitative analysis of cardiac myocyte relaxation: a simulation study". In: *Biophysical Journal* 90.5, pp. 1697–1722.

Nordsletten, D., S. Niederer, M. Nash, P. Hunter, and N. Smith (2011). "Coupling multi-physics models to cardiac mechanics". In: *Progress in Biophysics and Molecular Biology* 104.1-3, pp. 77–88.

Piazzesi, G., M. Reconditi, M. Linari, L. Lucii, P. Bianco, E. Brunello, V. Decostre, A. Stewart, D. B. Gore, T. C. Irving, et al. (2007). "Skeletal muscle performance determined by modulation of number of myosin motors rather than motor force or stroke size". In: *Cell* 131.4, pp. 784–795.

Quarteroni, A., L. Dede', A. Manzoni, and C. Vergara (2019). *Mathematical Modelling of the Human Cardiovascular System: Data, Numerical Approximation, Clinical*

Applications. Cambridge Monographs on Applied and Computational Mathematics. Cambridge University Press.

Regazzoni, F., L. Dedè, and A. Quarteroni (2018). "Active contraction of cardiac cells: a reduced model for sarcomere dynamics with cooperative interactions". In: *Biomechanics and Modeling in Mechanobiology*, pp. 1–24.

Regazzoni, F., L. Dedè, and A. Quarteroni (2019). "Machine learning of multiscale active force generation models for the efficient simulation of cardiac electromechanics". In: *MOX Report 33/2019, Politecnico di Milano*.

Regazzoni, F. (2019). "Mathematical modeling and efficient numerical simulation of the cardiac mechanical activation". PhD thesis. Politecnico di Milano.

Rice, J., G. Stolovitzky, Y. Tu, and P. de Tombe (2003). "Ising model of cardiac thin filament activation with nearest-neighbor cooperative interactions". In: *Biophysical Journal* 84.2, pp. 897–909.

Salvador, M., L. Dedè, and A. Quarteroni (2019). "An intergrid transfer operator using radial basis functions with application to cardiac electromechanics". In: *MOX Report 2019/36, Politecnico di Milano*.

Smith, D., M. A. Geeves, J Sleep, and S. M. Mijailovich (2008). "Towards a unified theory of muscle contraction. I: foundations". In: *Annals of Biomedical Engineering* 36.10, pp. 1624–1640.

Smith, N., D. Nickerson, E. Crampin, and P. Hunter (2004). "Multiscale computational modelling of the heart". In: *Acta Numerica* 13, pp. 371–431.

Sugiura, S., T. Washio, A. Hatano, J. Okada, H. Watanabe, and T. Hisada (2012). "Multi-scale simulations of cardiac electrophysiology and mechanics using the University of Tokyo heart simulator". In: *Progress in Biophysics and Molecular Biology* 110.2, pp. 380–389.

Ten Tusscher, K., D. Noble, P.-J. Noble, and A. V. Panfilov (2004). "A model for human ventricular tissue". In: *American Journal of Physiology-Heart and Circulatory Physiology* 286.4, H1573–H1589.

Ten Tusscher, K. H. and A. V. Panfilov (2006). "Alternans and spiral breakup in a human ventricular tissue model". In: *American Journal of Physiology-Heart and Circulatory Physiology* 291.3, H1088–H1100.

Ter Keurs, H., E. Hollander, and M. ter Keurs (2000). "The effect of sarcomere length on the force–cytosolic [Ca2+] relationship in intact rat cardiac trabeculae". In: *Skeletal muscle mechanics: from mechanics to function. Wiley, New York*, pp. 53–70.

Tortora, G. J. and B. H. Derrickson (2008). *Principles of anatomy and physiology*. John Wiley & Sons.

Washio, T., J. Okada, A. Takahashi, K. Yoneda, Y. Kadooka, S. Sugiura, and T. Hisada (2013). "Multiscale heart simulation with cooperative stochastic crossbridge dynamics and cellular structures". In: *Multiscale Modeling & Simulation* 11.4, pp. 965–999.

Washio, T., K. Yoneda, J. Okada, T. Kariya, S. Sugiura, and T. Hisada (2015). "Ventricular fiber optimization utilizing the branching structure". In: *International Journal for Numerical Methods in Biomedical Engineering*.

Zahalak, G. I. (1981). "A distribution-moment approximation for kinetic theories of muscular contraction". In: *Mathematical Biosciences* 55.1-2, pp. 89–114.

MOX Technical Reports, last issues

Dipartimento di Matematica
Politecnico di Milano, Via Bonardi 9 - 20133 Milano (Italy)

44/2019   Formaggia, L.; Gatti, F.; Zonca, S.
An XFEM/DG approach for fluid-structure interaction problems with contact

41/2019   Abbà, A.; Bonaventura, L.;   Recanati, A.; Tugnoli, M.;
Dynamical p-adaptivity for LES of compressible flows in a high order DG framework

42/2019   Martino, A.; Guatteri, G.; Paganoni, A.M.
hmmhdd Package: Hidden Markov Model for High Dimensional Data

43/2019   Antonietti, P.F.; Mazzieri, I.; Migliorini, F.
A space-time discontinuous Galerkin method for the elastic wave equation

39/2019   Lovato, I.; Pini, A.; Stamm, A.; Taquet, M.; Vantini, S.
Multiscale null hypothesis testing for network-valued data: analysis of brain networks of patients with autism

40/2019   Lovato, I.; Pini, A.; Stamm, A.; Vantini, S.
Model-free two-sample test for network-valued data

38/2019   Massi, M.C.; Ieva, F.; Gasperoni, F.; Paganoni, A.M.
Minority Class Feature Selection through Semi-Supervised Deep Sparse Autoencoders

36/2019   Salvador, M.; Dede', L.; Quarteroni, A.
An intergrid transfer operator using radial basis functions with application to cardiac electromechanics

37/2019   Menafoglio, A.; Secchi, P.
O2S2: a new venue for computational geostatistics

34/2019   Antonietti, P. F.; Mazzieri, I.; Melas, L.; Paolucci, R.; Quarteroni, A.; Smerzini, C.; Stupazzini,
Three-dimensional physics-based earthquake ground motion simulations for seismic risk assessment in densely populated urban areas